

Autonomous Discovery of Materials for Intercalation Electrodes**

Felix T. Bölle,^[a] Nicolai R. Mathiesen,^[a] Alexander J. Nielsen,^[a] Tejs Vegge,^[a] Juan Maria Garcia-Lastra,^{*[a]} and Ivano E. Castelli^{*[a]}

The development of automated computational tools is required to accelerate the discovery of novel battery materials. In this work, we design and implement a workflow, in the framework of Density Functional Theory, which autonomously identifies materials to be used as intercalation electrodes in batteries, based on descriptors like adsorption energies and diffusion barriers. A substantial acceleration for the calculations of the kinetic properties is obtained due to a recent implementation

of the Nudged Elastic Bands (NEB) method, which takes into consideration the symmetries of the system to reduce the number of images to calculate. We have applied this workflow to discover new cathode materials for Mg batteries, where two of these materials display a threefold increase in the potential of the Chevrel phase, the state-of-the-art cathode in commercial prototype Mg batteries.

1. Introduction

The prospects of substantial global warming calls for a transition towards a more sustainable energy infrastructure, based on the production of energy from renewable sources. Energy storage devices, e.g. rechargeable batteries, play a fundamental role in the transition from fossil fuels to renewable energy sources, as highlighted from the recent (2019) Nobel price in Chemistry awarded to Yoshino, Whittingham, and Goodenough.

Nowadays, Li-ion is the prevalent technology in electric vehicles and even used for stationary storage applications. While the concomitant development of portable electronics and that of the Li-ion technology are apparent, the ability of battery technologies to meet the necessary requirements cannot be taken for granted in other areas. Aside concerns on availability and cost of lithium and other critical raw materials (CRM), some general arguments could be raised against a potential generalized implementation of lithium based technology at large scale. Amongst the most promising alternative to Li-chemistries are the Na-ion batteries and analogous technologies based on multivalent cations like Mg^{2+} , Ca^{2+} , Zn^{2+} and Al^{3+} .^[1] The main drawback in Mg, Ca, Zn and Al batteries is related to the slow diffusion of multivalent elements, which drastically reduces the power performance. The foremost benefit is that for achieving a given capacity, the number of

ions needed are reduced by a factor equal to the ion valence. This turns out in less stressed electrode materials and seemingly less degradation upon cycling. Multivalent electro-positive metals include aluminum, zinc, calcium and magnesium. Aluminum, in spite of limited potential (2 V) and capacity (70 mAh/g) values.^[2] Regarding calcium, initial studies show fast rate capability.^[3] Arguably, the most interesting multivalent ion is magnesium, where significant progresses in performance has been achieved.^[1] The state-of-the-art cathode in commercial prototype Mg batteries is the Mo_6S_8 Chevrel phase, which is a covalent host where Coulombic interactions are reduced, favoring Mg ion diffusion.^[4] However, the potential achievable from this cathode is rather low (≈ 1 V vs Mg/Mg^{2+}). The discovery of novel cathode materials which can display higher potentials keeping, or even better improving, the ion diffusivity, is necessary to boost the Mg-ion technology.

Following an Edisionian "trial and error" approach to search for new materials is extremely time consuming and inefficient. During the last decades, quantum mechanical calculations, mostly within the framework of Density Functional Theory (DFT), have been efficiently used to predict properties and design novel materials for multiple applications. Recently, to accelerate the materials discovery, autonomous workflow schemes have been implemented,^[5–9] and more specifically for the discovery of battery materials, where a special focus was put on the kinetic properties, i.e. cation diffusivity.^[10,11] Including the kinetic aspect in an autonomous workflow is rather expensive and, in most cases, some approximations need to be done to compromise between accuracy and computational cost, e.g. pinball model^[12] or bond-valence calculations.^[11]

These workflows are usually based on generic tools that in addition to enable the complex inter-dependencies of the workflow steps allow for an easier reproducibility and provenance of the data.^[13,14] On one side, this helps researchers to share knowledge and expertise in the form of workflows, which

[a] F. T. Bölle, N. R. Mathiesen, A. J. Nielsen, Prof. T. Vegge, Asst. Prof. J. M. Garcia-Lastra, Asst. Prof. I. E. Castelli
Department of Energy Conversion and Storage, Technical University of Denmark, Anker Engelunds Vej 411, Building 301, DK-2800 Kgs. Lyngby, Denmark
E-mail: jmgla@dtu.dk
ivca@dtu.dk

** A previous version of this manuscript has been deposited on a preprint server (DOI: 10.26434/chemrxiv.9971054.v1)
An invited contribution to a Special Collection dedicated to the Symposium on Batteries and Supercapacitors at the E-MRS Spring Meeting 2019

can be reused by others as well as extended to include more features, and from the other they solve many issues^[15] related with consistency and reproducibility of the data. Workflows, in fact, enable the creation of consistent data sets by setting all the parameters at the beginning of the project and being consistent with them.

Most of the design for new materials proceeds through a 'funnel/sieve scheme', where at each steps materials, which do not fulfill the desired properties, are discarded. In addition, the complexity of the calculations and their simulation cost increases at each step. Examples of funnel schemes and workflows for, e.g., visible solar light ferroelectric devices can be found in the literature.^[16] In these cases, materials are selected for their stability, light harvesting properties, and interfaces. The discovery of battery materials is not dissimilar from these examples.

In this work, we establish an autonomous workflow to identify intercalation electrodes in batteries. Although we specifically search for novel cathodes for Mg batteries, the workflow is general enough to allow for the discovery of both cathode and anode electrodes for other battery technologies. In detail, the workflow is based on descriptors calculated at the DFT level, such as volume change upon charge/discharge, which gives information on the stability of the cathode, Mg adsorption energy, which indicates the open circuit voltage (OCV), and diffusion barriers, which is a descriptor for the ion mobility at different charge states. For the first time in a workflow, the kinetic aspects are kept at the DFT level of accuracy.

2. Workflow Overview

Figure 1 gives a schematic view of the seven main components of the workflow. The input from the user consists of choosing input parameters as well as providing a list of materials, i.e. compositions and structures, that will be investigated. Additionally, a database containing reference structures for the evaluation of the stability of an input structure on the convex hull is needed. The reference structures workflow is separated from the general workflow for finding ion-insertion cathode electrodes but ensures a consistent choice of input parameters for the reference calculations. Subsequently, the workflow autonomously takes care of generating and relaxing all needed structures necessary to determine crucial battery material properties. The three properties currently calculated are the stability (volume change upon charging/discharging and the thermodynamic stability), the electrode potential (Mg-adsorption energy) and the ion diffusivity (Mg-diffusion barriers). The two latter properties are evaluated both at a low and high state of charge (SOC). With respect to other work recently published,^[17] this workflow accelerates the calculations of the ion diffusivity by making use of symmetry considerations. In the following, the steps of the workflow are discussed in more detail. The workflow is interfaced with the Atomic Simulation Environment (ASE).^[18] Moreover, it is intended to work with the VASP DFT code,^[19–21] as well as with the workflow management system MyQueue.^[22] Efforts have been made to keep the workflow as general as possible in order to use the flexibility of ASE, which allows an interface with other DFT codes.

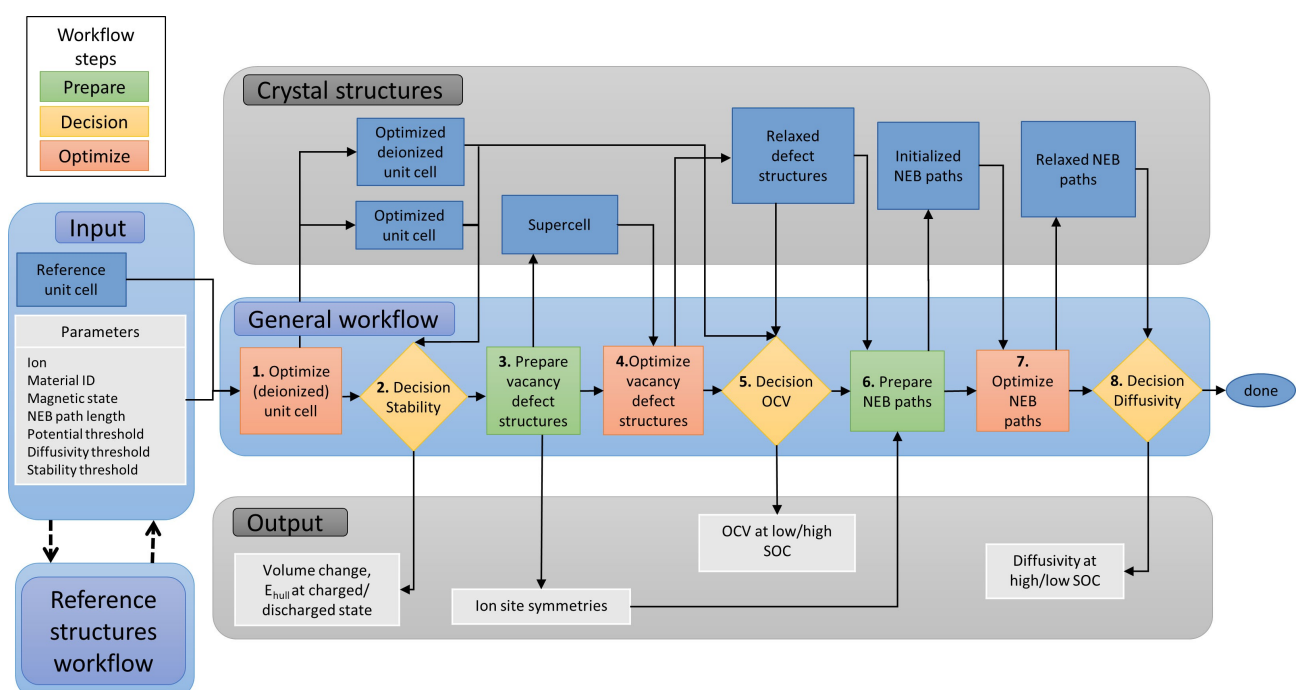


Figure 1. Structure of the workflow to identify suitable materials to be used as ion-insertion cathode electrodes in batteries. The workflow is divided into eight steps (middle row – General workflow). The steps prepare an optimization calculation (steps 3 and 6), optimize a structure (steps 1, 4 and 7) or check candidate materials for certain threshold values (steps 2, 5 and 8). The top row shows all the crystal structures created during the workflow given a reference unit cell, while the bottom row gives an overview of all the output generated. Once that the initial input is given (crystal structure and composition) and the parameters are set up, the workflow autonomously proceeds through all the steps.

2.1. User Input

In addition to the list of materials to investigate, the user needs to define 4 parameters:

- *ion*: The ion that will be studied which typically is an alkali or alkali-earth ion (i.e. Li, Na, K, Mg, or Ca).
- *material ID*: A unique identifier for each structure that is used to avoid duplicate calculations.
- *magnetic state*: The magnetic state parameter allows to study different magnetic starting configurations. This magnetic state is used for all structures throughout the workflow. The two options are the “non-magnetic” initialization or to initialize all ions “ferromagnetically”. The ferromagnetic initialization is carried out by initializing magnetic ions in a high spin state.
- *Nudged Elastic Band (NEB) path length*: The NEB path length determines the maximum linear distance between the initial and final site of the ion diffusing along the path. Paths that exceed this maximum length are neglected.

Three decision blocks are directly incorporated in the workflow scheme to decide whether to discard the candidate material or proceed with the calculations. The threshold values are given by the user deciding whether a material is suitable for further investigation or not, e.g. full computational OCV curve^[23] or experimental validation. These thresholds are the *Potential threshold*, which sets a requirement on the minimum average OCV, and the *Diffusivity threshold*, which favors the search for materials exhibiting low diffusion barriers (Figure 1). A *Stability threshold* can be given optionally by setting constraints on the maximum volume change upon discharging or the energy above the convex hull for the fully charged/discharged structures.

2.2. Calculations Steps

The potential materials investigated in the screening presented here are obtained from computational and experimental databases, such as the Materials Project,^[24] the Open Quantum Materials Database (OQMD),^[25] and Inorganic Crystal Structure Database (ICSD).^[26] All these materials have in common that the charge carrier (from now on, we explicitly write the charge carrier as Mg, although the workflow is not limited to identify cathode materials for Mg batteries) is present in the structure. Therefore, the starting structure of the workflow is always a fully discharged cathode material, from which we are going to remove magnesium. The workflow presented here is, however, more general and it could also be used to discover cathodes where the charge carriers are not present and intercalate in the interstitial sites.

2.2.1. Structure Optimization

The first step is to relax the input structure (with all Mg-ions, fully discharged state); the calculation details are discussed in Section 5. In parallel, we calculate the same structure where we

have removed all Mg-ions (deionized unit cell, optimized charged unit cell), as indicated in Figure 2. Both relaxations are carried out by the cell shape, volume and the atomic positions. From these two relaxations, it is possible to calculate the volume change in the charged and discharged states, which gives an indication on the mechanical stability of the battery. In addition, we relax a charged unit cell constraining its cell shape and volume. This is done by removing all Mg ions from the optimized discharged unit cell and scaling all atomic positions and the cell according to the ratio between the volume of the optimized charged unit cell and the optimized discharged unit cell, $r = V_{\text{charged}}/V_{\text{discharged}}$. Subsequently, all atomic positions are relaxed while keeping the cell shape and volume fixed. This structure, referred to as *discharged-constraint* unit cell, is used for the calculation of the OCV at a high SOC as it is explained in more detail in Section 2.2.5.

2.2.2. Decision Point 1-Stability

The volume change is calculated as [Eq. (1)]

$$\Delta V = \frac{V_{\text{charged}} - V_{\text{discharged}}}{V_{\text{discharged}}} \quad (1)$$

where $V_{\text{charged, discharged}}$ are the volumes of the unit cell with/without Mg-ions, respectively. The energy above the convex hull E_{hull} is evaluated for both structures giving an indication on the thermodynamic stability of the fully charged and discharged structures. Large energies above the hull will have implications on the structures cyclability and synthesizability and might lead to unwanted conversion reactions.^[27] On the other hand, due to kinetic stabilization metastable structures can still lead to the discovery of viable electrodes which makes it difficult to define a threshold value upfront.^[28,29]

2.2.3. Preparation of the Structures with Mg-Vacancies

To limit possible errors associated with defect-defect interactions, we need to create a supercell, which is obtained by repeating the relaxed unit cell from 2.2.1 until it satisfies the condition that the spacing between two vacancies is at least twice the NEB path length, defined in the user input. To ensure relatively fast calculations, we have added an additional requirement on the number of atoms in the supercell, which should not exceed 200 atoms. If this limit is reached, the workflow will automatically reduce the NEB path length (vacancy spacing) parameter to ensure that the maximum number of atoms in the supercell is not exceeded. To save computational time and retain symmetries, we assume that the supercell is fully relaxed after its creation. Subsequently, each of the symmetry-in-equivalent Mg ions is removed one-by-one from the supercell structure. The newly created defected structures, with one Mg vacancy, are analyzed by the Symmetry Equivalence Check tool, as implemented in ASE. The tool is based on the recipe as explained in Ref. [30]. Symmetry in-

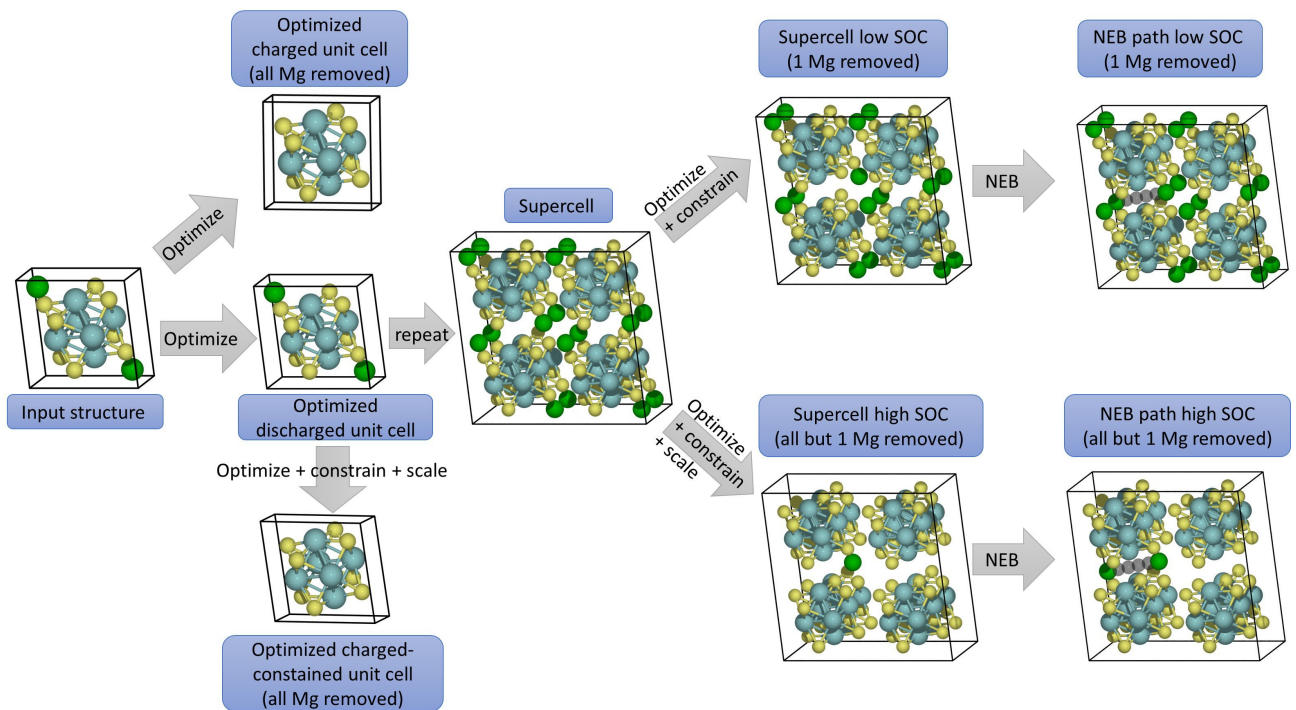


Figure 2. Structure creation throughout the workflow shown for the Chevrel Phase. The different labels on the arrows indicate how the resulting structure is obtained, i.e. *optimize*: Optimization of the cell shape, volume and atomic positions; *optimize + constrain*: Optimization of the atomic positions while keeping volume and cell shape unchanged; *optimize + constrain + scale*: Optimization of the atomic positions while re-scaling the volume according to the ratio $r = V_{\text{charged}}/V_{\text{discharged}}$ and keeping the cell shape fixed; *repeat*: solely repeating the cell; *NEB*: linear interpolation in between the initial and final site and subsequent optimization of the atomic positions while keeping cell shape and volume unchanged. Color coding: dark green (Magnesium), yellow (Sulfur), light blue (Molybdenum). The grey shaded spheres in the NEB path structures indicate the linear initialization of the NEB path and therefore the intermediate images. Both, initial and final site, are shown as dark green spheres.

equivalent sites are checked for percolating paths. Possible diffusion paths are only accepted if intermediate images obtained through linear initialization between initial and final images do not get closer than 1 Å to any atoms in the host structure. If combining all possible diffusion paths does not lead to percolating paths, i.e. the ion cannot traverse through the full structure, the selected ion occupying the site is non-conductive. In such cases the structure is discarded.

Once that the symmetry in-equivalent sites have been identified, a similar procedure is used to determine the symmetry in-equivalent NEB paths by removing the initial and final Mg site of the path from the structure. Checking for symmetry in-equivalent vacancy defect pairs (possible NEB paths) at this point of the workflow allows us to rank the materials according to the number of NEB calculations which need to be run. The Symmetry Equivalence Check tool identifies all the in-equivalent NEB paths that can be drawn between two Mg ions, which are spatially apart by less than the NEB path length value.

The output of this step of the workflow therefore consists not only of the supercell, but also of the information on the symmetry of the structure with respect to Mg-vacancies, which practically is a list of which Mg (or vacancy defect pairs) are symmetrically equivalent. Before continuing with the (heavy) optimization of the supercell, it is therefore possible to get a rough estimate of the number of NEB calculations that need to

be performed to evaluate the size of the diffusion barrier. The NEB paths are also checked for reflection symmetry at this point. Reflection symmetry will result in a less computationally expensive NEB calculation as will be explained in 2.2.6.

One problem that is frequently encountered is the correct labelling of defect sites. Indices of structures change as soon as vacancy defects are created. In order to work around this issue we tried to work with scaled positions of defects instead of specific indices whenever possible. If indices for specific sites were used (i.e. initial and final site in the NEB paths) they always match the indices in the created supercell.

2.2.4. Optimization of the Vacancy Defect Structures

The optimization of the vacancy defect structures is carried out for the dilute vacancy limit (low SOC) as well as for the high vacancy limit (high SOC). For the dilute vacancy limit, a single Mg-vacancy is created by removing only the symmetry in-equivalent ions from the supercell. In this case, the cell shape and volume is kept fixed during the relaxation and only the atomic positions are optimized. In the limit of high vacancy concentration, only a single symmetry in-equivalent Mg is left in the supercell and the supercell is scaled according to the ratio between the volume of the optimized charged unit cell and the optimized discharged unit cell, $r = V_{\text{charged}}/V_{\text{discharged}}$.

(see also Figure 2). Therefore, in the limit of high vacancy concentration, the shape and the volume of the supercell is fixed during relaxation and all atomic positions as well as lattice parameters are scaled. By keeping the cell shape fixed, the symmetries from the dilute vacancy limit case are preserved and the reflection symmetries have not changed. This enables to use the advantage of a reflection symmetry (reflective NEB) during the computationally expensive NEB calculations, as explained in 2.2.6. The assumption of a fixed cell shape even for the low Mg concentration limit will not hold in situations where a rather drastic change in cell shape upon charging occurs. On the other side, such materials would most likely break all contacts in a real battery and it should probably be discarded,^[31] irrespective. This could be checked already during step 2.2.1.

2.2.5. Decision Point 2-Minimum Voltage

The calculations performed so far allow us to calculate the potential at different SOCs, which is a descriptor for the minimum voltage of the cathode electrode. The different charge states include the low SOC (removing a single Mg from the supercell), calculated as [Eq. (2)]

$$V_{\text{low-SOC}} = \frac{(E_{\text{low-SOC}} + E_{\text{bulk-Mg}}) - E_{\text{discharged}}}{z} \quad (2)$$

where $E_{\text{discharged}}$ is the DFT energy of the relaxed unit cell, $E_{\text{low-SOC}}$ is the DFT energy of the supercell in the dilute vacancy limit, $E_{\text{bulk-Mg}}$ is the DFT energy of a single Mg atom in its most stable bulk structure and z is the amount of electrons transferred (in the case of Mg, $z = 2$), the high SOC (removing all but one ion from the supercell) calculated as [Eq. (3)]

$$V_{\text{high-SOC}} = \frac{(E_{\text{charged-constrained}} + E_{\text{bulk-Mg}}) - E_{\text{high-SOC}}}{z} \quad (3)$$

where $E_{\text{high-SOC}}$ is the DFT energy of the supercell in the high vacancy limit and $E_{\text{charged-constrained}}$ is the DFT energy of the deionized unit cell with the same cell shape as the supercell in the high vacancy limit but with a scaled volume. The last charge state considered is the average OCV calculated as [Eq. (4)]

$$V_{\text{average}} = \frac{(E_{\text{charged}} + n \cdot E_{\text{bulk-Mg}}) - E_{\text{discharged}}}{n \cdot z} \quad (4)$$

where E_{charged} is the DFT energy of the deionized unit cell and n is the amount of Mg ions in the discharged supercell.¹

2.2.6. Preparation of NEB Paths and Calculation of Diffusion Barriers

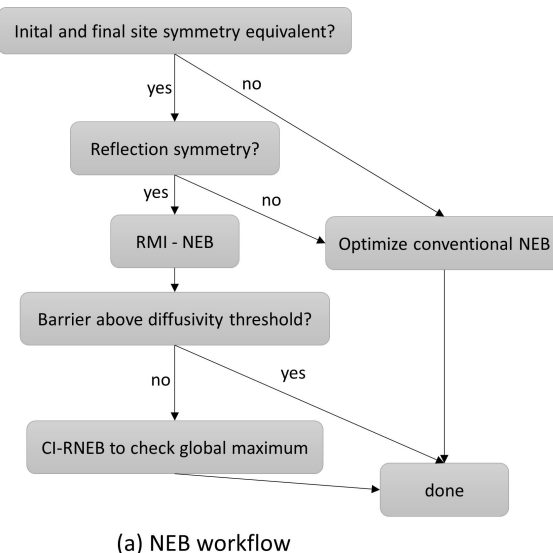
Methodologies to accelerate NEB calculations have been discussed in the literature. For instance, Rong *et al.*^[32] make use of an improved initial path guess over the usual linear initialization scheme and subsequently perform single point calculations on the images. They predict diffusion barriers that are within 20 meV compared to DFT calculations for Li systems. A different approach probes the potential energy surface (PES) using a gaussian process regression model to find the minimum energy path.^[33,34] In this work, we investigate the possibility of using the recently implemented Reflective-Nudged Elastic Band Method (R-NEB) for accelerating NEB calculations (see [17] for details about the implementation). In contrast to the two other methods, this does not approximate the PES but rather accelerates NEB calculations by considering symmetry operations to reduce the images to calculate.

The logic behind the preparation of the NEB path, in fact, decides which kind of NEB calculation to perform, as schematized in Figure 3 (a). All NEBs are run with ASEs internal NEB optimizer. We initialize the magnetic moments of all images using the information from the previously relaxed initial and final images. The total magnetic moment is forced to be the same in the initial and intermediate images. If no convergence is observed we remove the constraint of a fixed total magnetic moment and carefully inspect the structure visually after the workflow finishes for consistent magnetic moments.

The step 2.2.3 provides the necessary information about all the defect structures and their symmetries. A NEB path can be drawn by taking two of these structures, which are indicated as initial and final image. In case of the path not being reflective or the initial and final image not being symmetry equivalent, a conventional NEB is performed. We define a conventional NEB calculation as the process of setting up the initial and final structures followed by two separate relaxations of the initial and final image. After this, intermediate images, built through an interpolation of the initial and final relaxed structures, are added to the full path length (Figure 3 (b)).

If the initial and final image are symmetry equivalent the NEB path is tested for reflection symmetry. In three dimensions, the reflection symmetries can be reflective with respect to a plane (reflecting on one mirror plane), line (reflecting on two mirror planes), or point (reflecting on three mirror planes). If at least one reflection symmetry is found, we can perform a reflective-middle-image NEB (RMI-NEB) calculation. The RMI-NEB (sketched in Figure 3 (d)) is closely related to the Reflective NEB (R-NEB) method (sketched in Figure 3 (c)), which is also explained in Ref. [17]. In contrast to a conventional NEB where initial and final image are supplied, RMI-NEB needs only the initial image, as the final image can be created through symmetry operations from the initial image. This is schematically shown in Figure 3 (d) where the final image lies in the grey shaded area (dashed circle) indicating that the image has been created by symmetry operations rather than from a full DFT relaxation. Only one single image (middle image) needs to be calculated now. With respect to a conventional NEB run

¹ Note: These expressions are valid only if the energies are expressed in eV.



(a) NEB workflow

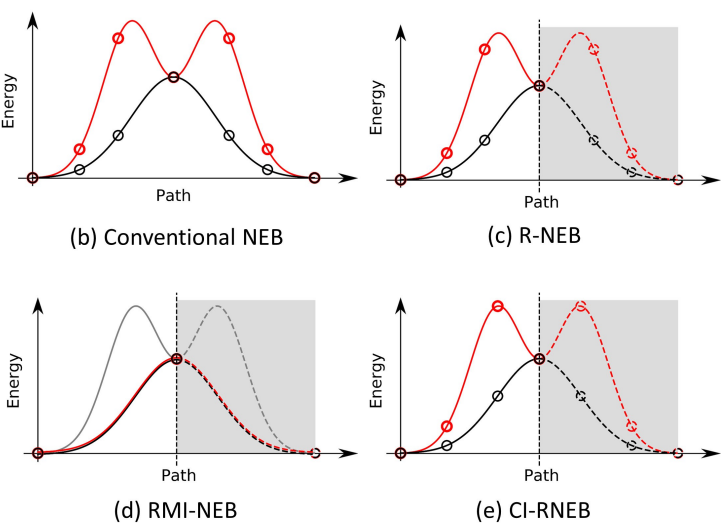


Figure 3. (a) Logic for the preparation of in-equivalent NEB paths by including reflection symmetry considerations, with the goal of reducing the computational time needed to find the transition state. The four figures to the right sketch the principles of the different ways of running a NEB calculation including a conventional NEB (b), reflective NEB or R-NEB (c), reflective-middle image NEB or RMI-NEB (d) and the climbing image reflective NEB or CI-RNEB (e). The images that lay in the grey shaded area indicate that these images are not calculated explicitly but are created by using symmetry operations. This is done by running a recent implementation of the NEB method [17]. The two colored lines show an example of a truly bellshaped energy barrier (black solid line) as well as an energy barrier with two maxima (red solid line).

with a single middle image, this improvement and speed-up here is that the relaxation of the final image is not needed. This speed-up is even more if several images are used for the NEB path. Consider a NEB path with five intermediate images (Figure 3 (b)). The reflective NEB (Figure 3 (c)) only considers three images including two intermediate images as well as the middle image. The two remaining intermediate images are then created by symmetry operations.

Using the approach of a single middle image, we always find an energy barrier that is smaller or equal to the energy of the transition state. For instance, it finds the correct transition state energy in case of a truly bellshaped barrier (Figure 3 (d)) solid black line) but it does not return the true height of the energy barrier in case of an energy barrier that has two maxima. Figure 3 (d) shows the true energy barrier curve with two maxima (grey line) as well as the found energy barrier curve with the RMI-NEB method in red that overlaps with the truly bellshaped energy barrier. An energy barrier with two maxima is rather common and can for example be found for the diffusion of Mg in Spinel structures,^[35] where the middle image corresponds to a configuration of the Mg ion in an octahedral site. In order to find the global maximum and the true height of the energy barrier in such example cases, we can subsequently run a climbing image reflective NEB (CI-RNEB), if the barrier is not already above the diffusion threshold value. Reflection symmetry is again applied by mirroring half of the intermediate images. The climbing image now finds the exact energy of the transition state for a barrier shape with two maxima (Figure 3 (e) solid red line). We stop the CI-RNEB in case we find all intermediate images to lie below the extracted maximum energy from the RMI-NEB, because this indicates that

the maximum energy barrier has already been found (black line, Figure 3 (e)).

We note that the initialization of the NEB paths is done by linear interpolation of two images. However, it is possible to follow different path initialization schemes, which might be preferred, especially when running a conventional NEB. For instance, the image dependent pair potential method providing an improved initial guess for the NEB path is already implemented in ASE requiring minimal changes in the code. In case of the reflective NEB paths, the user would have to make sure that the initialized path preserves the reflection symmetry which is not implemented in the presented workflow.

2.2.7. Decision Point 3-Ion Diffusivity and Data Collection

The final step of the workflow is to calculate the Mg diffusivity, which can be estimated from the Mg diffusion barriers obtained from the NEB method. At the end, all the structures, calculations, and estimated properties are collected and stored in a database.

2.3. Analysis of the Workflow

The workflow described here can be divided into three different layers, as indicated in Figure 4. The bottom layer contains scripts that directly interact with the calculation engine (VASP in this case) or other tools used to prepare and optimize the structures (ASE). Moreover, this layer includes all parameters used during the calculations, which are strictly connected with the simulation packages used. This layer is the least generic of

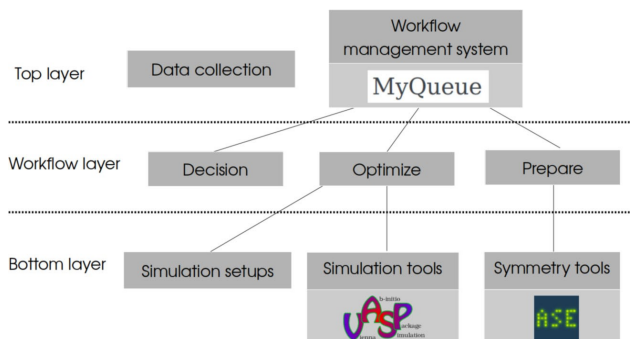


Figure 4. Different layers of the workflow.

the workflow, because it depends on the choice of code and parameters, decided by the user. This means that the middle layer of the workflow, or workflow layer, which contains the building blocks of the workflow, should allow the user to change any of the blocks of the bottom layer, e.g. the DFT code, without damaging all of the workflow structure. The workflow layer can be structured in three different blocks: a *prepare* block that prepares the structure to calculate and includes the logic to extract the symmetry equivalent structures; an *optimize* block that directly accesses the simulation tools and setups to optimize the various structures; and a *decision* block that acts at the decision points of the workflow and decides whether a material should be considered as a potential candidate for further calculations. The top layer consists of the workflow management system as well as the script to collect the generated data. Various workflow management systems have been implemented to be used in connection with materials science (e.g. AiiDA^[13] or Fireworks^[14]). In our case, we use an in-house tool called MyQueue,^[22] which deals with all the operations to submit (and resubmit failed) calculations as well as setting up the dependencies between the different steps of the workflow. Additionally, we included specific instructions on how to restart automatically failed or timed out calculations throughout the workflow similar to the CUSTODIAN package as implemented in Pymatgen.^[36]

3. Practical Application: Cathode Materials for Mg-ion Batteries

We used this workflow to find novel candidate materials to be used as cathodes in Mg-ion batteries. As the aim of this work is to describe the implementation of the workflow, we show, as a proof of concept, only a small subset of the possible materials that can be calculated.

Mo_6S_8 in the Chevrel phase (MgMo_3S_4 , shown in Figure 5 (a)) is currently the state-of-the-art for commercial prototype Mg cathodes as it can accommodate Mg^{2+} -ions for hundreds of cycles at stable potentials and charge capacities.^[4] This phase is chosen as the benchmark material and its diffusion and OCV properties provide the necessary input thresholds needed for the workflow.

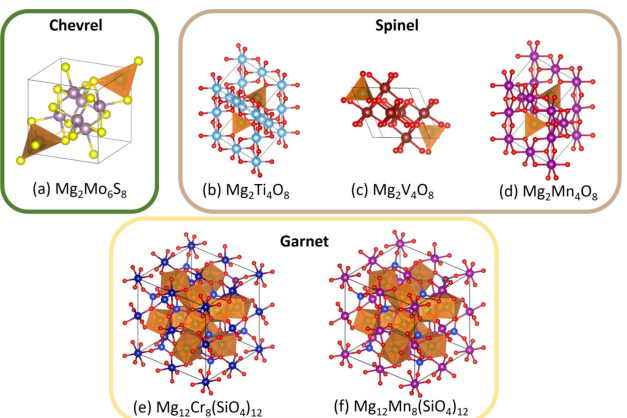


Figure 5. Unit cells of the six candidates investigated. The Mg^{2+} ions are inside the polyhedron to visualize differences in coordination. Shown are the Chevrel Phase, MgMo_3S_4 (a, Materials Project-ID: mp-677217); Spinel structures, MgB_2O_4 with $\text{B} = \{\text{Ti}, \text{V}, \text{Mn}\}$ (b: ICSD-65729, c: ICSD-60412, d: ICSD-290600); and Garnet structures, $\text{Mg}_3\text{B}_2(\text{SiO}_4)_3$ with $\text{B} = \{\text{Cr}, \text{Mn}\}$ (e: ICSD-77432, f: ICSD-27374). The Mg^{2+} ion occupies a tetrahedral site in structures (a-d). In the Garnet structures (e,f) Mg^{2+} has eight closest oxygen neighbors. The structures are visualized using VESTA.^[48]

3.1. Initial Pool of Materials to Investigate

We investigate only ternary and quaternary structures containing a transition metal, Mg and O. These structures are taken from the ICSD database.^[26] This choice is made to speed-up the synthesis of the identified materials as their synthetic pathway is established. Prior to running first principle investigations we apply filters that do not require the execution of DFT calculations. Metrics and design rules for finding fast magnesium conducting materials have been discussed extensively in literature (e.g. [37,38]). Based on these design rules, we only study materials where Mg is not in its preferred anion coordination environment in the interstitial site as large diffusion energy barriers are expected. The preferred anion coordination environment for a Mg^{2+} ion in crystallography literature has been determined to be six-fold.^[39] The coordination number of anions is determined using a Voronoi Tessellation of all atoms followed by discarding all anion neighbors that are more than 1.2 times the expected covalent ion-anion bond distance away from the Mg atom. In addition to the coordination number filter, only the structures without partial occupancy are considered. If the oxidation state of the transition metal inside the structure is exceeded upon fully charging the cathode material, the structure is excluded from the pool of starting candidates. A third filter criterion ensures that at least one percolating path for Mg exists in the structure prior to running the calculation. The structure is discarded in case all Mg ions are trapped. Less than 25 ternary and quaternary materials fulfill these criteria. In the present work, we consider a subset of 5 structures in addition to the benchmark material, which show reflection symmetry for the NEB paths. The benchmark material was taken from the Materials Project database^[24] due to the partial occupancy of magnesium in the structure from the ICSD database. All

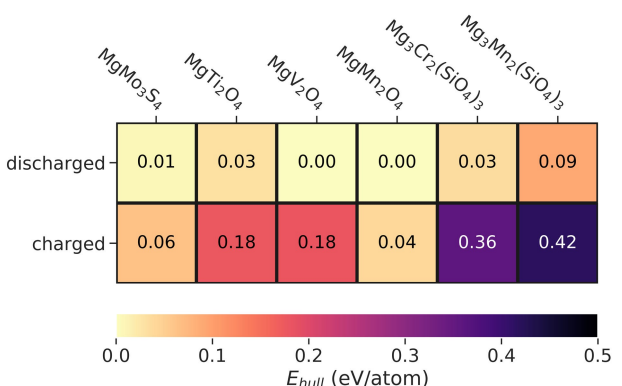


Figure 6. Thermodynamic stability of the charged and discharged phases. Reference structures for calculating the ground state hulls have been taken from the Materials Project database.^[24]

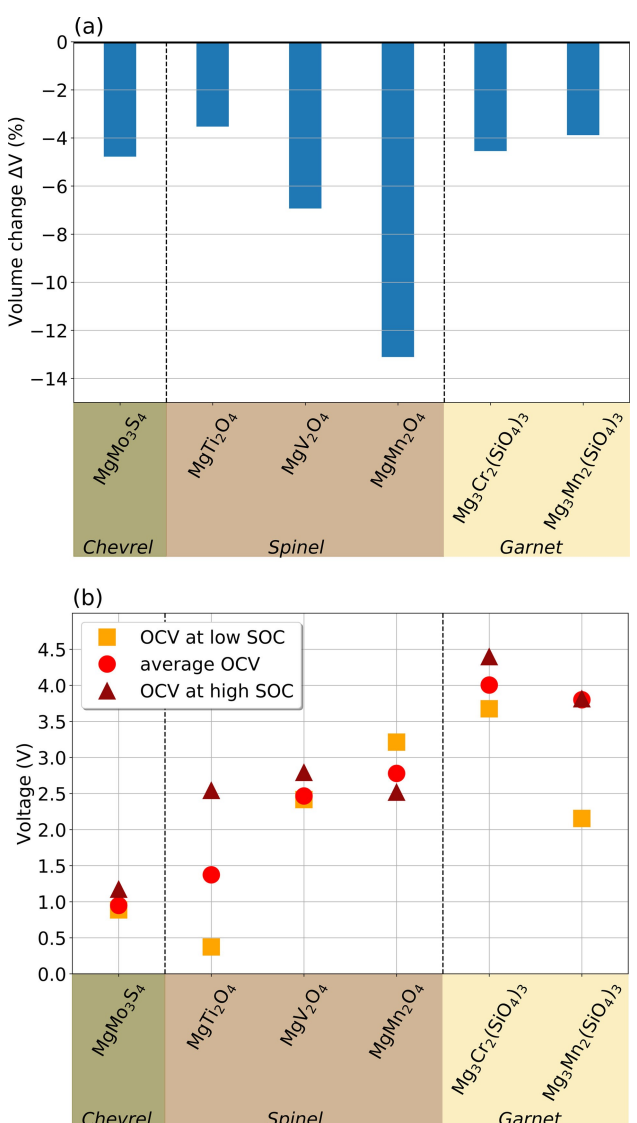


Figure 7. (a) Volume changes (in %) upon charging the cathode material as calculated using Eq. (1). (b) OCVs at different charge states calculated according to Eqs. (2), (3) and (4).

considered structures comprise three different crystal groups which are shown in Figure 5.

3.2. Results

The discharged structures in this study are known to exist and therefore show energies below 0.1 eV above the hull (Figure 6). For the charged structures especially the silicates exhibit larger energies above the hull of more than 0.4 eV. This might indicate poor stability upon charging the battery using this type of cathode as unwanted conversion reactions might occur. As expected, all materials show the tendency to reduce their volumes upon charging (Mg is removed), as shown in Figure 7 (a). The Manganese Spinel structure ($Mg_2Mn_4O_8$, Figure 5 (c)) shows the largest distortion among the studied materials. This has been already discussed in literature and has been referred to the filling of higher energy anti-bonding e_g orbitals for Mn upon reduction as the lower energy t_{2g} anti-bonding orbitals are fully occupied leading to larger volume changes (this is not the case for other elements, such as Ti, for which free lower energy t_{2g} orbitals can be occupied).^[35,40]

The OCVs indicate that all materials have a higher average OCV than the Chevrel phase (Figure 7 (b)). The voltages lie in between a range of 1.3–4.5 V making these materials interesting as Mg cathodes as the OCV is higher than the benchmark material. The only exception is $MgTi_2O_4$ (Figure 7 (b)), which has a calculated voltage below the average voltage of the Chevrel phase at a low SOC. Since all materials fulfill the first requirement (average OCV larger than the OCV for the Chevrel phase), we proceed with investigating the Mg-diffusion using NEBs.

The barriers calculated for the benchmark material $MgMo_3S_4$ are ~750 meV at a low SOC and ~940 meV at a high SOC (Figure 8(a) + (b)). They suggest that the multivalent Mg^{2+} -ions are more mobile at a low SOC, i.e. a structure with a high concentration of Mg^{2+} . The Chevrel phase is the only material that has its transition state barrier at the middle image for the high and low SOC structures. This means that in this case evaluating the barriers using the RMI-NEB method results in the same barriers as obtained using the CI-RNEB method. The Spinel structures ($MgTM_2O_4$, TM={Ti, V, Mn}) show low transition state barriers at the middle images (~30–420 meV). Higher mobility is again observed at a low SOC in agreement with what has been found in recent NEB studies on Spinel structures (e.g. $MgMn_2O_4$ in [35]). Although these barriers are significantly lower than the ones for the benchmark material, the transition state is not found at the middle image which becomes obvious when looking at barriers obtained using a climbing image in Figure 8 (b) (~320–660 meV). NEB calculations reported in the literature indicate a barrier shape with two maxima, as can be seen in Ref. [35]. The RMI-NEB method thus fails to find such a global maximum (as described in details above, Figure 3 (d)). The reason behind this shape of the barrier is the diffusion topology, which results in the Mg^{2+} -ion diffusing from an initial tetrahedral site through an octahedral intermediate coordination to its final site which is also tetrahedral. In the case of $MgTi_2O_4$, the intermediate octahedral

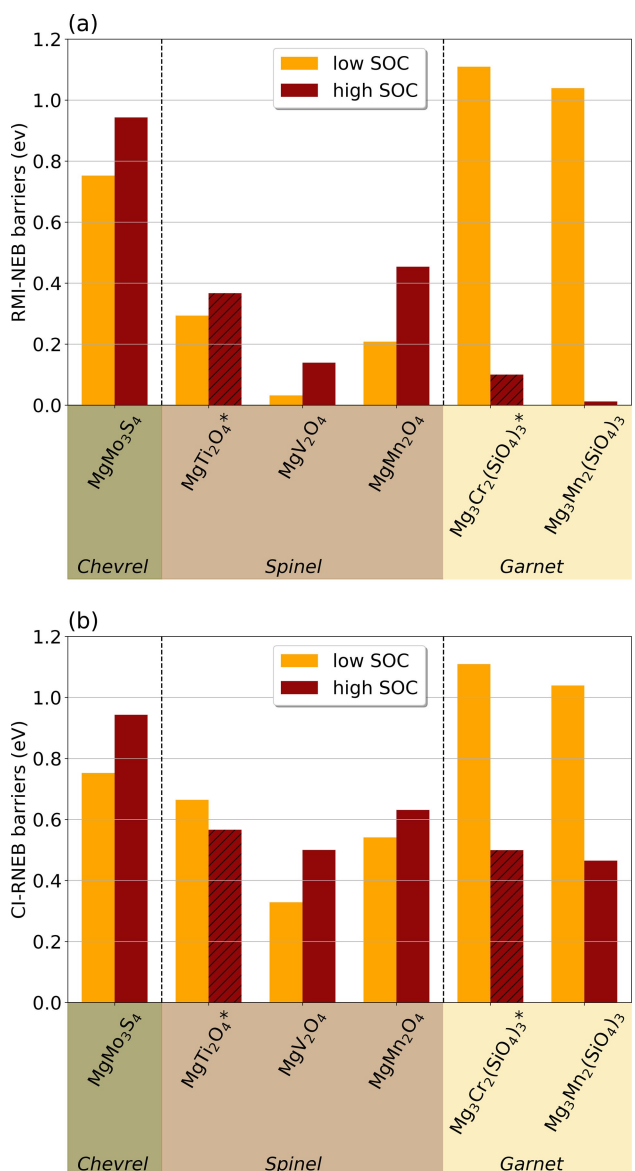


Figure 8. Height of the diffusion barrier calculated using the RMI-NEB/CI-RNEB method. Only a single intermediate image (middle image) is used to determine the transition state for the RMI-NEB method. The CI-RNEB path consists of five intermediate images including the reflected and middle images. The hatched bar for materials marked with an asterisk (*) indicates that the middle image is lower in energy than the initial and final state.

site has a lower energy than the initial and final tetrahedral site. This is indicated by formulas marked with an asterisk and the hatched bar in Figure 8. This suggests that the pathway should start from the octahedral site and not from the tetrahedral sites.^[35] Experimental studies on the cubic thiospinel structure Ti_2S_4 find partial occupancies of Mg in octahedral and tetrahedral sites.^[41] These findings might also apply to the oxide spinel Ti_2O_4 studied here.

The two silicate structures ($Mg_3TM(SiO_4)_3$, TM = {Cr, Mn}) have low transition state barriers at the middle images for a high SOC (below ~100 meV, where the middle image of $Mg_3Cr(SiO_4)_3$ is again lower in energy than the initial image). The barriers found using the CI-RNEB are again larger, indicating

the transition state does not coincide with the middle image of the path. The diffusion is significantly slower at a low SOC, as shown by the higher transition state energy barrier above 1 eV. This is similar to olivine structures studied in the literature ($FePO_4$)^[37] which also show larger diffusion barriers for moving multivalent ions at a low SOC compared to the diffusion barriers at a high SOC. By investigating the middle image from the RMI-NEB calculation and comparing the middle image at a low and high SOC, we note that at a high SOC, less Mg^{2+} -ions compete to attract the negatively charged O^{2-} -anions. The Mg–O bonds between the diffusing Mg^{2+} -ion and its closest oxygen neighbors are approximately 10% shorter for the middle image in the high SOC, compared to the low SOC case, which leads to a more stabilized structure and therefore a lower barrier. The lower transition state barrier might also be a result of the rather unstable charged phase of the silicates (E_{hull} in Figure 6). A more detailed study on the stability and possible conversion reactions is probably needed.

Within the same crystal symmetries, the materials show similar trends for the height of the diffusion barriers: the Garnet structures show a significantly slower diffusion of Mg^{2+} upon discharging whereas the diffusion barriers of the Spinels are much closer in energy for the high and low SOCs. This indicates that calculating diffusion barriers (and their shapes) for a few representative structures from each crystal group can be a useful approach to accelerate the materials discovery. These trends can be used to select the most promising crystal structures to study using the workflow proposed here. The energy barriers for a single diffusing Mg-ion in the studied oxide systems are thus governed by the diffusion path, which is specific for each crystal symmetry, as already reported in the literature.^[37] In contrast, the OCV and volume changes are governed by the Red-Ox properties of the transition metal.

4. Conclusions and Perspective

We have presented a workflow based on DFT calculations, which autonomously identifies candidate materials to be used as intercalation electrodes in batteries. The workflow is composed of different steps, where the volume change and thermodynamic stability upon charging, the OCV at different charge states and the NEB diffusion energy barrier at high and low SOC are calculated. This workflow has been tested to identify possible cathode materials for Mg batteries, which can improve the performance (faster Mg^{2+} diffusion and higher OCVs) of the Chevrel phase; the most common cathode material in Mg batteries. In addition to identifying candidate materials, the workflow can provide quick insights, useful to investigate trends that can even further accelerate the discovery of novel materials. The workflow is continuously developed and may be accessed at <https://gitlab.com/asc-dtu/workflows/ion-insertion-battery-workflow>. The structures presented in this work are available on FigShare.^[42]

We would like to point out that the workflow is a useful tool for an autonomous screening approach that gives insights in diffusion properties of materials, since calculating diffusivities

is typically the most expensive part computationally, as well as manually going through and setting up the calculations. The workflow is not a universal tool for studying any cathode material and so far it only works for materials that have the cation inside the structure. We are currently working on extending it to include the following features:

- The workflow is not able to find the correct magnetic state ordering for all structures. Initializing all magnetic ions in a high spin state lead to satisfactory convergence for the materials shown but also failed to find the correct spin state for specific cases. We are currently working on finding a more automated way to find the correct magnetic ordering leading to the minimum energy configuration.
- Until now we only removed Mg ions from a structure that had the ion already inserted. It is in principle also possible to include structures where Mg is added into the interstitial sites and feed that structure to the workflow presented here. This would enable us to study crystal systems like 2-D layered structures without making changes to the workflow.

Computational Details

The computational details refer to the example described here in section 3.5, and can easily be modified. All calculations have been performed using the Vienna Ab-initio Simulation Package (VASP) using a plane-wave basis set.^[19–21] The exchange and correlation effects are approximated using the Perdew-Burke-Ernzerhof revised for solids (PBEsol) functional.^[43] An energy cut-off of 520 eV was applied to describe the valence electrons. Sampling the Brillouin zone is done using a k-point density $>4.7 \text{ \AA}^{-1}$. As a required convergence criterion all forces on the movable nuclei had to be less than 0.03 eV/ \AA . To account for the self interaction error in the d orbitals of the transition metal oxides a +U correction is applied with the values taken from the Material Project database, i.e. $U_V = 3.25 \text{ eV}$, $U_G = 3.7 \text{ eV}$, $U_{Mn} = 3.9 \text{ eV}$.^[24,44] In the calculation for the convex hull, the reference for oxygen in the gas phase is approximated using the approach suggested by Rossmeisl *et al.*,^[45] where the energy of oxygen at 0 K is calculated as the difference in energy of water and hydrogen molecules in gas phase, including the zero point energy (ZPE) corrections.

All NEB simulations^[46] have been calculated using the GGA-PBEsol functional. The R-NEB method was applied^[17] as implemented in the Atomic Simulation Environment package (ASE),^[18] whenever reflection symmetry in the path is observed. As a required convergence criterion all forces had to be less than 0.05 eV/ \AA . The +U correction penalizes the energy of the transition state since it is a less localized state than the initial and final state. Thus, we do not apply a +U correction to the NEB calculation as also discussed in Ref. [35]. The distance between repeating defects in the super cells is always larger than 9 \AA to avoid defect-defect interaction errors.

Acknowledgement

The authors wish to acknowledge support from the “European Magnesium Interactive Battery Community (e-Magic)” FET-Proactive project (Contract N. 824066). FTB, TV, IEC acknowledge support from the Department of Energy Conversion and Storage, Technical University of Denmark, through the Special Competence

Initiative “Autonomous Materials Discovery (AiMade)”.^[47] NRM and JMGL acknowledge support from the Villum Foundation’s Young Investigator Programme (4th round, project: *In silico design of efficient materials for next generation batteries*. Grant number: 10096).

Conflict of Interest

The authors declare no conflict of interest.

Keywords: Mg-Batteries • Autonomous discovery • Workflow • Cathodes • Density Functional Theory

- [1] J. Muldoon, C. B. Bucur, T. Gregory, *Chem. Rev.* **2014**, *114*, 11683–11720.
- [2] S. K. Das, S. Mahapatra, H. Lahan, *J. Mater. Chem. A* **2017**, *5*, 6347–6367.
- [3] A. Ponrouch, M. Palacin, *Curr. Opin. Electrochem.* **2018**, *9*, 1–7.
- [4] A. Mitelman, M. Levi, E. Lancry, E. Levi, D. Aurbach, *Chem. Commun.* **2007**, *41*, 4212–4214.
- [5] K. Tran, A. Palizhati, S. Back, Z. W. Ulissi, *J. Chem. Inf. Model.* **2018**, *58*, 2392–2400.
- [6] J. H. Montoya, K. A. Persson, *npj Comput. Mater.* **2017**, *3*, 14.
- [7] S. Hastrup, M. Strange, M. Pandey, T. Delmann, P. S. Schmidt, N. F. Hinsche, M. N. Gjerding, D. Torelli, P. M. Larsen, A. C. Riis-Jensen, *et al.*, *2D Mater.* **2018**, *5*, 04002.
- [8] N. Mounet, M. Gibertini, P. Schwaller, D. Campi, A. Merkys, A. Marrazzo, T. Sohier, I. E. Castelli, A. Cepellotti, G. Pizzi, *et al.*, *Nat. Nanotechnol.* **2018**, *13*, 246.
- [9] K. Kuhar, A. Crovetto, M. Pandey, K. S. Thygesen, B. Seger, P. C. K. Vesborg, O. Hansen, I. Chorkendorff, K. W. Jacobsen, *Energy Environ. Sci.* **2017**, *10*, 2579–2593.
- [10] L. Kahle, A. Marcolongo, N. Marzari, *arXiv preprint arXiv:1909.00623*, 2019.
- [11] N. A. Katcho, J. Carrete, M. Reynaud, G. Rousse, M. Casas-Cabanas, N. Mingo, J. Rodríguez-Carvajal, J. Carrasco, *J. Appl. Crystallogr.* **2019**, *52*, 148–157.
- [12] L. Kahle, A. Marcolongo, N. Marzari, *Physical Review Materials* **2018**, *2*, 065405.
- [13] G. Pizzi, A. Cepellotti, R. Sabatini, N. Marzari, B. Kozinsky, *Comput. Mater. Sci.* **2016**, *111*, 218–230.
- [14] A. Jain, S. P. Ong, W. Chen, B. Medasani, X. Qu, M. Kocher, M. Brafman, G. Petretto, G.-M. Rignanese, G. Hautier, D. Gunter, K. A. Persson *Concurrency and Computation: Practice and Experience* **2015**, *27*, 5037–5059.
- [15] L. M. Ghiringhelli, C. Carbogno, S. Levchenko, F. Mohamed, G. Huhs, M. Lüders, M. Oliveira, M. Scheffler, *npj Comput. Mater.* **2017**, *3*, 46.
- [16] I. E. Castelli, T. Olsen, Y. Chen, *J. Phys.: Energy* **2019**, *2*(1), 011001.
- [17] N. R. Mathiesen, H. Jonsson, T. Vegge, J. M. Garcia Lastra, *J. Chem. Theory Comput.* **2019**, *15*, 3215–3222.
- [18] A. H. Larsen, J. J. Mortensen, J. Blomqvist, I. E. Castelli, R. Christensen, M. Dulak, J. Friis, M. N. Groves, B. Hammer, C. Hargas, E. D. Hermes, P. C. Jennings, P. B. Jensen, J. Kermode, J. R. Kitchin, E. L. Kolsbjerg, J. Kubal, K. Kaasbjerg, S. Lysgaard, J. B. Maronsson, T. Maxson, T. Olsen, L. Pastewka, A. Petersen, C. Rosgaard, J. Schiøtz, O. Schütt, M. Strange, K. S. Thygesen, T. Vegge, L. Vilhelmsen, M. Walter, Z. Zeng, K. W. Jacobsen, *J. Phys. Condens. Matter* **2017**, *29*, 273002.
- [19] G. Kresse, J. Furthmüller, *Phys. Rev. B* **1996**, *54*, 11169.
- [20] G. Kresse, D. Joubert, *Phys. Rev. B* **1999**, *59*, 1758.
- [21] P. E. Blöchl, *Phys. Rev. B* **1994**, *50*, 17953.
- [22] J. Mortensen, M. Gjerding, K. Thygesen, *J. Open Source Softw.* **2020**, *5*(45), 1844.
- [23] Y. S. Meng, M. E. Arroyo-de Domípablo, *Energy Environ. Sci.* **2009**, *2*, 589–609.
- [24] A. Jain, S. P. Ong, G. Hautier, W. Chen, W. D. Richards, S. Dacek, S. Cholia, D. Gunter, D. Skinner, G. Ceder, K. A. Persson, *APL Mater.* **2013**, *1*, 011002.
- [25] J. E. Saal, S. Kirklin, M. Aykol, B. Meredig, C. Wolverton, *JOM*, **2013**, *65*, 11, 1501–1509.
- [26] <http://www.fiz-karlsruhe.com/icsd.html>.

- [27] P. Canepa, G. Sai Gautam, D. C. Hannah, R. Malik, M. Liu, K. G. Gallagher, K. A. Persson, G. Ceder, *Chem. Rev.* **2017**, *117*, 4287–4341.
- [28] D. C. Hannah, G. Sai Gautam, P. Canepa, G. Ceder, *Adv. Energy Mater.*, **2018**, *8*, 1800379.
- [29] I. E. Castelli, T. Olsen, S. Datta, D. D. Landis, S. Dahl, K. S. Thygesen, K. W. Jacobsen, *Energy Environ. Sci.* **2012**, *5*, 5814–5819.
- [30] D. C. Lonie, E. Zurek, *Comput. Phys. Commun.* **2012**, *183*, 690–697.
- [31] L. Beaulieu, K. Eberman, R. Turner, L. Krause, J. Dahn, *Electrochem. Solid-State Lett.* **2001**, *4*, A137–A140, 2001.
- [32] Z. Rong, D. Kitchaev, P. Canepa, W. Huang, G. Ceder, *J. Chem. Phys.* **2016**, *145*, 074112.
- [33] O.-P. Koistinen, F. B. Dagbjartsdóttir, V. Ásgeirsson, A. Vehtari, H. Jónsson, *J. Chem. Phys.*, **2017**, *147*, 152720.
- [34] J. A. G. Torres, P. C. Jennings, M. H. Hansen, J. R. Boes, T. Bligaard, *Phys. Rev. Lett.* **2019**, *122*, 156001.
- [35] M. Liu, Z. Rong, R. Malik, P. Canepa, A. Jain, G. Ceder, K. A. Persson, *Energy Environ. Sci.* **2015**, *8*, 964–974.
- [36] S. P. Ong, W. D. Richards, A. Jain, G. Hautier, M. Kocher, S. Cholia, D. Gunter, V. L. Chevrier, K. A. Persson, G. Ceder, *Comput. Mater. Sci.* **2013**, *68*, 314–319.
- [37] Z. Rong, R. Malik, P. Canepa, G. Sai Gautam, M. Liu, A. Jain, K. Persson, G. Ceder, *Chem. Mater.* **2015**, *27*, 6016–6021.
- [38] P. Canepa, S.-H. Bo, G. S. Gautam, B. Key, W. D. Richards, T. Shi, Y. Tian, Y. Wang, J. Li, G. Ceder, *Nat. Commun.* **2017**, *8*, 1759.
- [39] I. Brown, *Acta Crystallogr. Sect. B* **1988**, *44*, 545–553.
- [40] C. A. Marianetti, D. Morgan, G. Ceder, *Phys. Rev. B* **2001**, *63*, 224304.
- [41] X. Sun, P. Bonnick, V. Duffort, M. Liu, Z. Rong, K. A. Persson, G. Ceder, L. F. Nazar, *Energy Environ. Sci.* **2016**, *9*, 2273–2277.
- [42] <http://www.https://doi.org/10.11583/DTU.11627178>.
- [43] G. I. Csonka, J. P. Perdew, A. Ruzsinszky, P. H. Philipsen, S. Lebégue, J. Paier, O. A. Vydrov, J. G. Ángyán, *Phys. Rev. B* **2009**, *79*, 155107.
- [44] L. Wang, T. Maxisch, G. Ceder, *Phys. Rev. B* **2006**, *73*, 195107.
- [45] J. Rossmeisl, A. Logadottir, J. K. Nørskov, *Chem. Phys.* **2005**, *319*, 178–184.
- [46] G. Henkelman, B. P. Uberuaga, H. Jónsson, *J. Chem. Phys.* **2000**, *113*, 9901–9904.
- [47] <http://www.aimade.org>.
- [48] K. Momma, F. Izumi, *J. Appl. Crystallogr.* **2011**, *44*, 1272–1276.

Manuscript received: October 11, 2019

Revised manuscript received: December 18, 2019

Accepted manuscript online: January 16, 2020

Version of record online: March 3, 2020